A wireless power transfer mattress based system for perpetually operating physiological monitoring wearables

Zhiqiang Xu, *Student Member, IEEE* and Esther Rodriguez-Villegas

***Abstract*— This paper presents a novel wireless power mattress-based system architecture tailored to guarantee continuous energy for in-home environment healthcare wearables intended to be used in the context of patients who would benefit from long-term monitoring of specific physiological biomarkers. The design demonstrates that it is possible to transfer over 20mW at a primary-secondary distance of 20.7cm, whilst still keeping within all FCC/ICNIRP safety regulations, using the proposed simplified beamforming-controlled power transfer multi-input single-output system. Compared with other beamforming-controlled based works, the proposed design used non-coupling coil arrays, significantly reducing the algorithmic complexity. An on-chip wireless power charger system was also designed to provide high-efficiency power storage (89.3% power conversion efficiency and 83.9% power charge efficiency), guaranteeing wearables can continuously maintain their functionality. In contrast with conventional NiMh chargers, this work proposes a trimming function that makes it compatible with batteries of varying capacities. It also employs a four-stage charge loop to ensure safety and sustainability during the charging process. Overall, this work shows that by relying on wireless power transfer, it is, in principle, possible to create a safe wearable that could enable continuous monitoring of certain healthcare biomarkers with little or zero maintenance burden for the patients or carers.**

***Index Terms*— Array signal processing, non-coupling coil system, electromagnetic compatibility (EMC), wireless power transmission, analogue integrated circuit design.**

I. Introduction

As the world population ages, the prevalence of chronic conditions, such as cardiovascular, respiratory or neurological diseases, are on the rise [1]. Over time, it is not uncommon for patients to become dependent on both professional and family-led care [2]. Continuous monitoring of physiological parameters of patients at home would be highly beneficial in a variety of healthcare scenarios in the context of these diseases. Having unobtrusive, low-maintenance devices to do this, however, would be important both to increase patients' compliance/adherence to their use and to minimise the workload of carers. Wearables have an important role to play in this context because they don't impose an additional physical burden on patients. However, a drawback of being wireless is the fact that they need to be frequently charged which leads to discontinuation of use.

In recent decades, there has been increasing research on wireless power transfer (WPT) applications for implantable and wearable devices, aiming to enable long-term physiological monitoring [3], [4]. These devices typically encompass a variety of physiological sensing modalities, such as photoplethysmography (PPG), electrocardiogram (ECG), thermometers, and accelerometers. Their power requirements range from nanowatts to milliwatts, depending on the desired data accuracy and sampling rates [5], [6]. Although most devices operate at low power levels and emit minimal radio frequency (RF) radiation, concerns regarding human exposure to RF radiation and its potential harmful effects on human health persist. To ensure compliance with safety regulations and guidelines and minimise any potential risks, a specific absorption rate (SAR) is established as a metric to measure the amount of RF energy absorbed by the human body [7]. Compliance with SAR limits is essential to prevent tissue heating and mitigate health risks associated with excessive RF energy absorption. However, simple SAR measurements and evaluations are not sufficient to ensure compliance with Federal Communications Commission (FCC) Electromagnetic Compatibility (EMC) regulations, as human tissue has complex and varying characteristics [8]. In addition to the potential heat damage caused by RF radiation, it is crucial to assess the safety of human exposure to RF radiation in accordance with the guidelines of the International Commission on Non-Ionizing Radiation Protection (ICNIRP) [9]. This assessment is based on the concept of Maximum Permissible Exposure (MPE), which defines the maximum level of RF radiation exposure considered safe for humans. The MPE takes into account factors such as the resonant frequency of the radiation, the duration of exposure, and the specific body part exposed to the radiation. The ICNIRP exposure limits are generally more stringent than the FCC safety limits, and hence they are preferentially applied in most countries [10]. Apart from the safety considerations, the current state-of-the-art wearables with WPT functionality are limited by the physical properties of electromagnetic waves [11]. Many conventional devices can only achieve wireless

This work was supported in part by the European Research Council under Grant 724334.

Z. Xu and E. Rodriguez-Villegas are with Wearable Technologies Lab, Department of Electrical and Electronic Engineering, Imperial College London, SW7 2BT, United Kingdom. E-mail: {zhiqiang.xu18, e.rodriguez}@imperial.ac.uk

power delivery within a restricted distance and position (typically around a few centimetres) and require precise alignment. As the power delivery distance increases, the power transfer efficiency (PTE) rapidly decreases [12], [13]. Despite the robustness of their power management design, these devices need frequent recharging, which hinders their ability to provide continuous physiological monitoring.

Recently, a few works on self-capacitance-based (SC-based) WPT systems have demonstrated the capability to achieve high-efficiency power delivery over comparatively long distances, regardless of misalignment [14], [15]. These works explored the possibility of transmitting milliwatts across the body, having the power source on one side and the wearable on the other, using the body's tissues surfaces as the medium for transmission. It was demonstrated that the PTE only experienced a linear decrease as the distance was reduced. Although this is certainly very innovative and promising the risks associated to both, the electromagnetic and usability hazards associated to having the wired power source in contact with the body need further investigation.

Several recent works have also introduced a multiple-input single-output (MISO) approach utilizing specialized coil structures to achieve a uniform power distribution across a wide power transfer area, mitigating misalignment issues and enabling the efficient delivery of energy to devices [16], [17]. However, it has been noted that some of these approaches lack consideration for compliance with ICNIRP exposure limits, which might make them potentially unsuitable for practical biomedical applications. In contrast, Reepa and colleagues addressed these concerns by developing an on-body cluster-based MISO system that successfully delivered over 100mW power to implants [18]. Importantly, their approach adhered to both ICNIRP exposure limits and standard Specific Absorption Rate (SAR) limits, ensuring safety and compliance. Nevertheless, the requirement for multiple coils to wrap around the body makes it impractical for patients to wear over extended periods of time, and could potentially create additional hazards. Meanwhile, uniform power distribution generated by the system may cause a waste of energy if the receiver could only appear in one place at once. Besides the coil optimizations, some state-of-the-art works focused on improving power transfer methods, like the beamforming-controlled power transfer, to adaptively control multi-coil systems to deliver beamformed power waves to devices compensating for device misalignment over a wide range [19], [20]. The beamforming approach focuses on delivering optimised power within a limited specified power budget. As long as the power budget is specified to meet all safety regulations and compliance, the beamforming approach could emerge as an alternative solution for wearables used in continuous physiological monitoring applications on patients.

This work addresses several challenges and explores the feasibility of designing a fully qualified and compliant mattress-based physiological monitoring system that allows patients to avoid frequent energy depletion of their health devices and achieve long-term sustainable vital monitoring. The paper is organised as follows: Section II outlines user scenarios, potential user interactions, and system specifications based on these scenarios; Section III introduces a novel beamforming-controlled power transfer (BCPT) coil subsystem for the mattress-based system, designed to achieve mid-range transfer distances even with device misalignment. The subsystem enhances PTE by phase-controlling the coil array and reduces system complexity by using a heterogeneous non-coupling coil array; Section IV focuses on optimising the mattress-based system's performance to comply with FCC EMC regulations and safety requirements; Section V presents a high-efficiency on-chip wireless power charger (WPC) designed for a 2.4V Nickel-metal Hydride (NiMH) rechargeable battery, providing details on its improvements, performance, and reliability. When combined with the BCPT coil subsystem, the entire system can avoid energy depletion and enable continuous operation of devices worn or implanted in patients. Section VI provides results for both the PCB-manufactured BCPT and the tape-outed WPC, validating the reliability and feasibility of uninterrupted physiological monitoring for patients; finally, Section VII concludes the paper.

II. System Overview

The overall system architecture, as depicted in Fig. 1, comprises a mattress-based BCPT subsystem for optimised power delivery to wearables, and an on-chip WPC that adaptively charges the rechargeable battery, ensuring reliable performance. A 12.7cm foam mattress, compliant with the minimum thickness requirements for hospital-grade mattresses [21], was utilised for the experiments.

In the BCPT subsystem, four primary coils were positioned beneath the mattress, and four corresponding relay coils were embedded within it. A secondary coil harvests the beamformed RF energy from the primary coils. A power control unit with a microcontroller is used to process the BCPT algorithm and

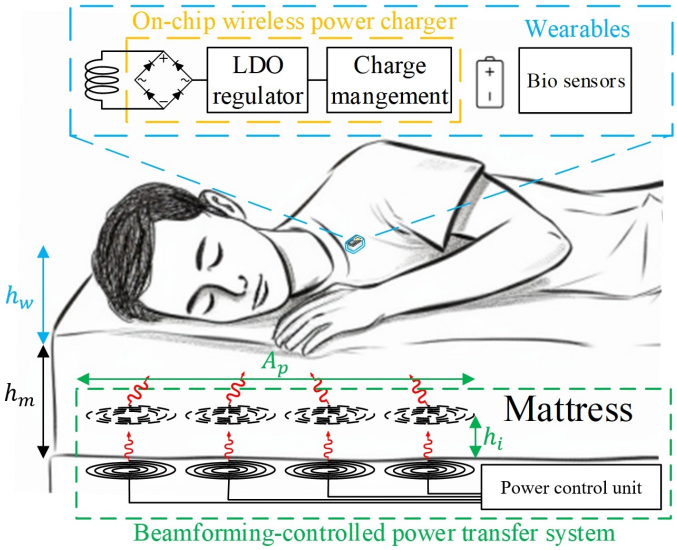

Fig. 1. System overview of the proposed mattress-based wireless power charge system (h_w is the height of the wearable over the mattress, h_m is the mattress thickness, h_i is the insert height of the relay coil in the mattress and A_p is the power area covered by BCPT subsystem).

control coils in real time. In this work, 6.78MHz is chosen as the operating frequency because it is the lowest frequency band allowed by the Industrial, Scientific and Medical (ISM) regulation and complies with the Airfuel Alliance Standard for mid-range power transfer applications [22]. Moreover, following the SAR equation in (7), there is less energy absorbed by the human tissue at the lower frequency, which is important since the human body consists of 65% to 70% of water and can be easily heated up from dozens of megahertz [23]. Besides, the BCPT subsystem takes into account the FCC EMC and safety compliance regulations.

In the WPC subsystem, a 2.4V 16mAh NiMH battery was used as the wearables' external energy source. This choice was made because NiMH batteries have lower cell voltage than Lithium-Ion batteries of equivalent capacity, which results in greater power efficiency for low-power RF systems (5V I/O) without significant voltage dropout in high-voltage circuits. Additionally, NiMH batteries are robust and stable because of the fewer active chemical materials they contain and do not catch fire upon impact. Meanwhile, Li-ion batteries require additional protection circuits to ensure their safe operation [24]. Hence, NiMH batteries do provide a very attractive powering alternative for wearables for their long-term monitoring purposes.

III. Beamforming-Controlled Power Transfer Subsystem

Similar to traditional beamforming technologies in the domain of communications, BCPT technologies focus on power delivery by controlling multiple primary coils to direct their transmission waves toward secondary coils. This approach effectively enhances the system PTE and achieves a longer transmission distance spanning tens of centimetres [19]. The principle behind BCPT involves tracking the magnetic channels (mutual coupling) between primary and secondary coils and subsequently determining the corresponding transmission configurations (amplitude and phase) for each primary coil to enable in-phase power transmission and energy concentration on the secondary coil for the improved PTE [20]. Inspired by it, the proposed BCPT subsystem involves a non-coupling heterogeneous coil array [25] to further enhance PTE and reduce algorithm processing complexity. This subsystem controls four primary coils to transmit corresponding in-phase energy waves to the secondary coil, while four relay coils are utilised to enhance PTE over an extended distance. Moreover, the novel non-coupling coil array helps simplify beamforming-control algorithm processing. This is further explained in subsequent subsections. Subsection III-A discusses the design of the non-coupling coil, while subsection III-B presents the simplified beamforming-control algorithm.

A. Non-coupling coil design

Before introducing the non-coupling coil design, to ease understanding, the equivalent circuit for a conventional single-input-single-output (SISO) coil system is presented, as shown in Fig. 2, together with its equations that serve to illustrate how to measure the magnetic channel. They are derived as follows.

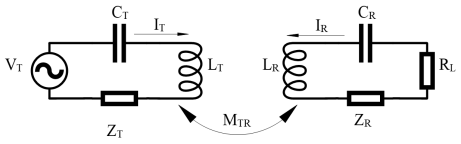

Fig. 2. A equivalent circuit of a SISO WPT system.

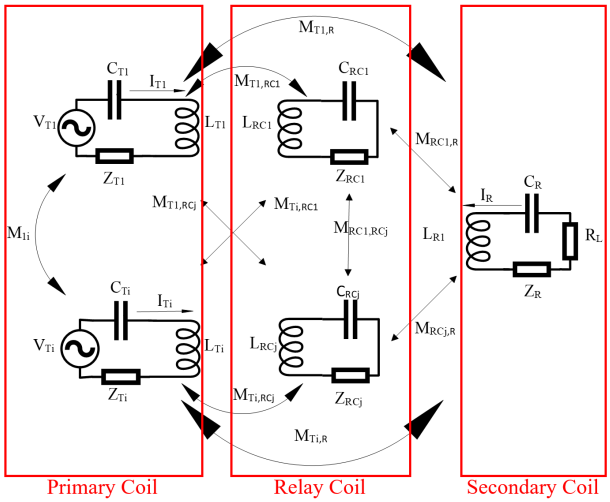

Fig. 3. A equivalent circuit of a MISO WPT system with relays.

$$V_T = I_T Z_T - j\omega M_{T,R} I_R \tag{1}$$

$$I_R(Z_R + R_L) = j\omega M_{T,R} I_T \tag{2}$$

where V_T, I_T, C_T, L_T, Z_T represent the voltage, current, capacitance, inductance and impedance of the primary coil, respectively, and $V_R, I_R, C_R, L_R, Z_R, R_L$ represent the voltage, current, capacitance, inductance, impedance, and load of the secondary coil, respectively. When the secondary coil approaches the near-field of the primary coil, the magnetic channel $M_{T,R}$ induces a current I_R on the secondary side and this affects the electrical parameters on the primary side. The relationship between a single primary coil and a single secondary coil is shown in (1) and (2). Therefore, estimating the magnetic channel based on the electrical parameters variations on the primary coil is achievable, and this will be elaborated upon in subsection. III-B.

However, analytically estimating the magnetic channel in a MISO system with four primary coils, four relay coils and a secondary coil is complex, if crosstalk is taken into account. Crosstalk also makes it a challenge to match the impedance for all coils since every single impedance matching step brings new crosstalk components affecting other coils' impedance in the array. The equivalent circuit diagram of a MISO coil system is shown Fig. 3, and the corresponding equation is derived below.

$$V_{T1}=I_{T1}Z_{T1}-\sum j\omega M_{T1,T_i} I_{T_i}-\sum j\omega M_{T1,RC_j} I_{RC_j}-j\omega M_{T1,R} I_R \tag{3}$$

$$I_R(Z_R+R_L)=\sum j\omega M_{Ti,R} I_{T_i}+\sum j\omega M_{RC_j,R} I_{RC_j} \tag{4}$$

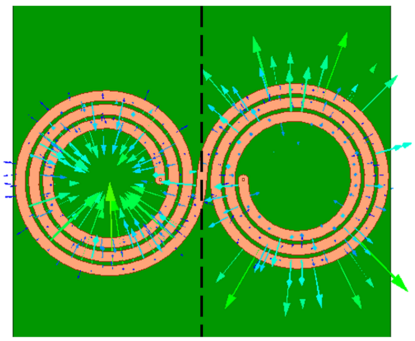

Fig. 4. Coil geometry of a single non-coupling heterogeneous coil with its E-field vector plots.

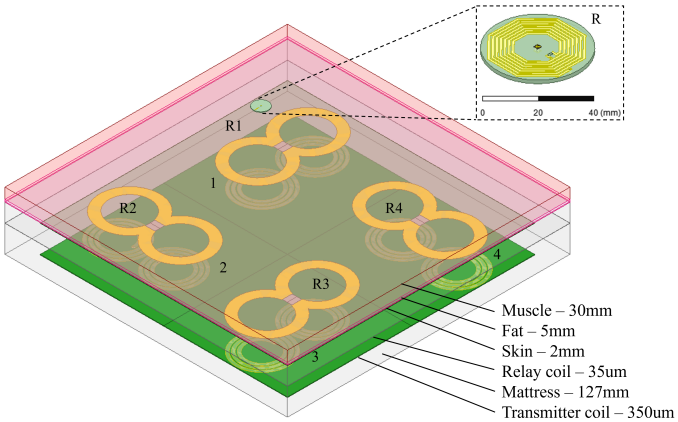

Fig. 5. Mattress-based BCPT subsystem.

where $V_{T_i}, I_{T_i}, I_{RC_j}$ represent the voltage and current in the i-th primary coil and the current in the j-th relay coil, respectively. $M_{T1,T_i}, M_{T1,RC_j}, M_{Ti,R}, M_{RC_j,R}$ represent the magnetic channel between a single primary coil 1 and the i-th primary coil, a single primary coil and the j-th relay coil, the i-th primary coil and the secondary coil, and the j-th relay coil and the secondary coil, respectively. From (3), three magnetic channels connect with a single primary coil. Apart from the direct power channel with the secondary coil $M_{T1,R}$, the primary coil suffers from crosstalk with other primary coils, with respect to $j\omega M_{Ti,R} I_{T_i}$. Meanwhile, the power loss caused by the uniform power distribution to irrelevant relay coils, M_{T,RC_j} is equally severe. Hence, a non-coupling coil design is introduced below to solve the crosstalk issues.

This work's coils were designed with heterogeneous coil geometry for their specific negligible coupling, or as referred to in [26], "non-coupling" property. Each heterogeneous coil consisted of two identical but opposite poles. When fed with a power source, two inverse currents flowing along their corresponding pole generate completely inverted electromagnetic fields around the two poles. As shown in Fig. 4, the vector of the electrical field (E-field) points inside and outside the poles, respectively. Hence, it leads to the corresponding produced magnetic field (H-field) with the same field strength but in the opposite direction, perpendicular to the E-fields, cancelling their magnitude at the cancellation plane (black dot line in Fig. 4). By properly placing the second coil aligned in the cancellation plane, their crosstalk can be effectively eliminated, as there is no H-field interaction in this plane. Similarly, four non-coupling heterogeneous primary coils were placed in the same plane, as shown in Fig. 5, in order to cancel the crosstalk from their neighbour coils in the array. It is worth mentioning that different geometries of the non-coupling coil array were discussed in [25]. The one chosen in this work is more area-efficient and has less design complexity than other geometries discussed in [25].

Considering the significant power attenuation as the transmission distance increases, the relay coil array was inserted in the mattress to help maintain a reliable power delivery over 20.7cm, and it was designed to be a non-coupling coil in order to minimise the crosstalk with nearby coils. As a result, each primary coil and its corresponding relay coil can be treated as a primary-relay (TxR) unit, which greatly reduces the measurement circuit size and also the BCPT algorithm complexity. Hence, equations (3) and (4) can be simplified as below.

$$V_{TxR} = I_{TxR} Z_{TxR} - j\omega M_{TxR} I_R \tag{5}$$

$$I_R(Z_R + R_L) = j\omega M_{TxR} I_{TxR} \tag{6}$$

where V_{TxR},I_{TxR},Z_{TxR} are the voltage, current and impedance of the TxR unit, respectively. M_{TxR} is the magnetic channel between the TxR unit and the secondary coil. The geometry of the relay coil was optimised with one turn and wide tracks to minimise the wire resistance, so that it was able to be self-resonant with one parallel capacitor whilst maintaining a high Q factor for better transmission performance over a relative long distance.

The structure of the mattress-based BCPT subsystem is shown in Fig. 5 and its electric properties (@6.78MHz) in Table I. Since the primary-relay coil does not have direct contact with the human tissue, its coil specifications were optimised to maximise the Q-factor in order to achieve higher PTE, with no safety risk due to heat. A secondary coil was designed to be an octagonal planar spiral coil. The topology as well as size-strictly limited to a radius of 2cm were constrained by the realistically available space within a miniature wearable device. The octagonal shape was chosen for its higher filler factor (the difference between outer and inner diameter over the sum of outer and inner diameter) to achieve a higher Q-factor within the SAR limit. SAR is defined in (7) and must remain below a peak level of 1.6 W/kg over 1 gram of localised tissue [27].

$$SAR = \frac{\sigma |E|^2}{\rho} \tag{7}$$

In (7), σ is the conductivity of human tissue at the corresponding resonant frequency, E is the total electrical field strength in the form of root-mean-squared, and ρ is the density of human tissue.

Meanwhile, since it is wearable work, an additional 1mm plastic ABS shield was added between the human tissue and the secondary coil to downgrade the electromagnetic exposure from the secondary coil to the tissue. It was also to provide mechanical support for the devices. The SAR level on the upper part of the body was 0.33W/kg. As shown in Fig. 6,

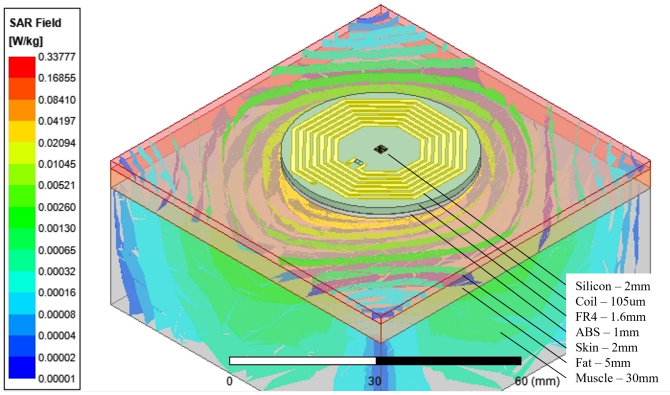

Fig. 6. The receiver on the equivalent human tissue model with its SAR field plots, assuming receiving a maximum power of 100mW.

TABLE I
ELECTRIC PROPERTIES OF MATERIALS IN ANSYS HFSS SIMULATION.

Material	Electrical Conductivity (S/m)	Relative Permittivity (ε_r)	Loss Tangent ($tan\delta$)
Air	-	1.006	-
Copper	58000000	1	-
FR4 epoxy	-	4.4	0.02
PCB laminate, Polyamide (PI)	-	4.25	0.014
Plastic, ABS	-	2.99	0.004243
Silicon	-	11.9	-
Foam, polyurethane	9.976e-12	1.07996	0.0001789
Skin (dry)	0.147	478	0.8153
Fat (average infiltrated)	0.0496	3.5	37.5712
Muscle	0.602	233	6.8499

this was obtained by simulating in the extreme scenario when the receiver is on the body (taking into account the wearable closure made of ABS), and also assuming the secondary coil receives a maximum power of 100mW. The received power range is sufficient for the wearable to operate, whilst preventing damage to tissue, since the power requirement would be less than 10mW.

The detailed coil specifications for primary, relay and secondary coils are shown in Table II. The equivalent human tissue model (2mm skin, 5mm fat and 30mm muscle) is from the IT'IS Foundation database [28] and was integrated with the simulation to optimise the performance with respect to safety.

B. Algorithm for beamforming-controlled power transfer

The introduced BCPT subsystem was employed to provide optimized voltage amplitude and phase adjustments to each primary coil. The goal was to enhance the PTE at the secondary coil. The algorithm independently manages each primary coil. Real-time monitoring of each transmitter coil is performed to establish their respective magnetic channels with the secondary coil. By doing this, the relative secondary coil position can be estimated and the power level in the corresponding primary coil can be adjusted. If the receiver is far from the transmitter-relay coils, the system would detect a lack of coupling and reduce the power level of the corresponding transmitter coils. The power budget of the

TABLE II
SPECIFICATIONS OF NC PRIMARY COILS, NC RELAY COILS AND THE SECONDARY COIL.

Coil Parameter	Transmitter	Relay	Receiver
Turns	3	1	7
Outer radius	$75mm$	$75mm$	$20mm$
Inner radius	$39mm$	-	$8.8mm$
Width	$8mm$	$27mm$	$0.9mm$
Turns spacing	$4mm$	-	$0.7mm$
Thickness	$350\mu m$	$35\mu m$	$105\mu m$
Inductance	$2979.7nH$	$98.4nH$	$1567.8nH$
Resistance	$285.2m\Omega$	$11m\Omega$	$390.6m\Omega$
Q factor	445.1	379.6	171.0

coil system and the non-coupling coil array configurations follows both SAR, near-field and far-field E&H field radiation requirements as per FCC & ICNIRP regulations and hence the safety constraints have been taken into account in the design. Meanwhile, utilizing the configuration of the non-coupling primary-relay coil array, only four primary-relay units were equipped with measurement circuits. This is in contrast to needing eight separate measurement circuits for both primary and relay coils. This design choice significantly simplified the system's complexity, both algorithms and circuits.

The beamforming algorithm is based on detecting the magnetic channel between the transmitter-relay coils and the receiver. As the receiver enters the near field of the transmitter-relay array, they are mutually coupling and the transmitters' electric parameter (voltage, current and impedance) are affected. By monitoring this difference at the transmitter array side, the complete coupling information can be calculated and adapted to control the power level and phase of the transmitter. This is explained in detail in Equations (5) to (6) and (8) to (17). Furthermore, the functionality of the beamforming algorithm is shown in this subsection.

The key parameter for the BCPT algorithm, corresponding to the magnetic channels, was estimated by obtaining the measured differences on the TxR side. When the secondary coil is present, and coupled with the TxR unit, the electrical state (V, I, R) of the TxR unit will be affected as a function of the strength of the magnetic channel. As per (5), $V_{TxR} = I_{TxR}Z_{TxR} - j\omega M_{TxR}I_R$, the voltage of the TxR unit changes because of the effect from the current of the secondary coil, induced via the magnetic channel. As the impedance of the TxR changes, this can be obtained by the measurement circuits. Applying $Z'_{TxR} = V_{TxR}/I_{TxR}$ in (5), the induced current I_R can be rearranged into (8), which shows the dependency with I_{TxR}. Furthermore, substituting (8) into (6), the magnitude of the magnetic channel M can be calculated as:

$$I_R = \frac{I_{TxR}(Z'_{TxR} - Z_{TxR})}{j\omega M_{TxR}} \tag{8}$$

$$M^2_{TxR} = \frac{(Z'_{TxR} - Z_{TxR})(Z_R + R_L)}{\omega^2} \tag{9}$$

The sign of the magnetic channel is obtained in the same way. The first TxR is set as the reference coil with the positive sign of its magnetic channel. When measuring the magnetic channel of the first TxR, other TxRs are turned off, but there is

some induced voltage from the secondary coil and also the first TxR, as expressed in (10). By rearranging (10), the sign of the magnetic channel between the i-th TxR and the secondary coil can be calculated as below. The magnetic channel's magnitude and sign for other TxRs can be calculated similarly.

$$V_{TxRi} = j\omega M_{TxRi} I_R + j\omega M_{TxR_{1i}} I_{TxR1} \tag{10}$$

$$\text{Sign}(M_{TxRi}) = \text{Sign}(\frac{V_{TxRi} - j\omega M_{TxR_{1i}} I_{TxR1}}{j\omega I_R}) \tag{11}$$

In the implemented system, the input power fed to the TxR was limited to 1.6W. Hence the total power budget for TxR and the secondary coil was constrained as represented in (12). To find an analytical optimised solution for the maximum harvested power at the secondary coil side, (13) has to be solved under the condition of (12), following the specified power budget. I_R can be replaced by HI_{TxRi} from (6), where H and I_{TxRi} are simplification matrices for calculation and are shown below in (15) and (16).

$$P_{total} = P_{TxR} + P_R = I_R^2(Z_R + R_L) + \sum I_{TxRi}^2 Z_{TxRi} \tag{12}$$

$$i_{TxR-BF} = \arg\max((H^* i_{TxR}^*)(Z_R + R_L)(H i_{TxR})) \tag{13}$$

$$i_{TxR-BF} = \beta \cdot \text{maxeig}(H^*(Z_R + R_L)H) \tag{14}$$

$$H = \frac{j\omega}{Z_R + R_L}[M_{TxR1}, M_{TxR2}, M_{TxR3}, M_{TxR4}] \tag{15}$$

$$i_{TxR-BF} = [I_{TxR1}, I_{TxR2}, I_{TxR3}, I_{TxR4}] \tag{16}$$

β is a constant normalised value related to initial primary-relay electrical parameters. It is obtained by substituting the beamforming current i_{TxR-BF} into the initial power constraint (12) of the system before applying the beamforming. Its detailed derivation can be found in [20]. Finally, the beamform-controlled input for each TxR can be obtained by applying (17) below.

$$V_{TxRi} = \beta(M_{TxRi}(Z_{TxRi} + \frac{\omega^2(M_{TxR1}^2 + M_{TxR2}^2 + M_{TxR3}^2 + M_{TxR4}^2)}{Z_R + R_L})) \tag{17}$$

IV. Biomechanical Consideration and FCC Regulations

The proof-of-concept mattress-based system in this work was designed targeting uninterrupted physiological monitoring for patients confined to a single bed. A large-scale primary-relay coil array comprising eight coils, each with a diameter of 15 cm, was placed under or inserted into the mattress. The goal was to deliver at least 10 mW to a potential wearable worn by the patient whilst considering a realistic range of relative positions/motion within the bed. However, a large-scale coil array transmitting dozens of milliwatts over a mid-range up to 20 cm can easily exceed the safety limits of human exposure regulation. Hence, this section investigates the feasibility of delivering sufficient power to operate the wearable over an extended distance using a relay coil array with optimised position and power area, while also adjusting the transmit power to meet the FCC EMC regulatory and safety compliance regulations.

In other words, a performance tradeoff exists between PTE and safety levels. Identifying the optimal placement of the relay coil array is essential for efficient power delivery to the receiver. As known from section III-A, inserting the relay coil array into the mattress can effectively improve the PTE. Here, considering the cost of customised mattress fabrication, this work simplifies subsequent real experiments by splitting the mattress into two parts: a topper mattress and a bottom mattress, maintaining the total thickness. Furthermore, when inserting the relay coil array into the mattress, the depth of sinkage experienced by the patient while sleeping is considered. If the relay coil array's insert position is too close to the mattress surface, the patient's mattress sinkage could cause deformation of the relay coils, resulting in PTE performance degradation and discomfort for the patient. In this work, three different system designs taking into account primary-relay coil array placements are investigated aiming to optimise the PTE performance whilst still complying with FCC safety regulations. The three variants are: (a) With a priamry coil array placed under the mattress without relay coils; (b) With transmitter coil array placed under the mattress with relay coil array inserted into the mattress at a height of 51 mm; (c) With transmitter coil array placed under the mattress with relay coil array inserted into the mattress at a height of 76 mm.

TABLE III
FCC EMC REGULATORY AND SAFETY COMPLIANCE REGULATIONS FOR ALL WEARABLES AT 6.78MHz

Regulation @6.78MHz	Limits
SAR @whole body	0.08W/kg
SAR @partial body	1.6W/kg
SAR @hands, wrists, feet and ankles	4.0W/kg
MPE @H-field	0.72A/m
MPE @E-field	271.68V/m
Far-field E-field emission	15uV/m

According to the RF radiation exposure limits in the FCC regulations (47 CFR 1.1310), RF radiation safety compliance to human tissue at 6.78MHz must be guaranteed to be within both SAR and MPE limits. The SAR limits of this work on the primary-relay coil array do not need to be investigated in depth since it is safe to assume, considering the transmission power, distances and the lack of contact with the body, that these will not be exceeded. This work does however investigate the MPE as a function of the location of the coils as well as the electromagnetic characteristics of the different designs. This is important because excessive ionising radiation can cause permanent, irreversible damage to biological tissue, including DNAs, hence the reason for regulatory bodies, including the FDA to impose limits on them [29]. The MPE limits at 6.78MHz for both E-field and H-field are defined in (18) and (19).

$$H(A/m) = \frac{4.89}{f(MHz)} = 0.72A/m \tag{18}$$

$$E(V/m) = \frac{1842}{f(MHz)} = 271.68V/m \tag{19}$$

Furthermore, the far-field performance of the electronic devices should be considered because it can potentially cause interference to other devices. The far-field distance is defined from twice the wavelength to infinity, and is specified in

FCC regulations (47 CFR 15.223) for devices that operate in bands between 1.705MHz and 10MHz. Especially for this work using coils with high-quality factors and operating at a narrow band, the generated electrical field strength shall not be higher than 15μV/m at a distance of 30 meters. The relevant FCC EMC regulatory and safety compliance limits are listed in Table III. The simulation results for the different system architectures and the performance tradeoffs discussion are shown in section VI-A.

V. On-chip Wireless Power Charger System

This section presents a high-efficiency approach for storing energy and providing a stable power supply for long-term monitoring purposes. A fully-on-chip high-efficiency tunable wireless power charger was designed catering for most mA-level NiMH batteries. It is described in two parts, the RF power harvesting module and the charging control module. The overall system block diagram is shown in Fig. 7.

Considering the variability in the relative distances between primary coils and secondary coils, a conventional RF application invariably requires over-voltage protection to avoid damage to the receiver unless the power budget is limited on the transmitter side. At the top chip design level a conventional way of avoiding damage caused by potential transitory high voltage/current levels is to have electrostatic discharge (ESD) clamps in all I/O pads, which do allow for high current to flow to the power rail rather than going into the core devices. However, the standard ESD clamp does not necessarily work for RF applications since the RF signal strength that could reach the transistors instantaneously and continuously could be far above the breakdown voltage of the devices. Moreover, the performance of RF applications can be heavily determined by impedance matching since this can effectively reduce the power reflection from critical ports avoiding degradation in transmission performance. Standard ESD clamps that are made of large-sized diode-connected transistors commonly have too large parasitics to optimise on this. Another aspect to consider with transitory large inputs is the fact that subsequent rectifiers would need to be able to accommodate for those, which would make their design significantly harder leading to unnecessary overheads in terms of power consumption.

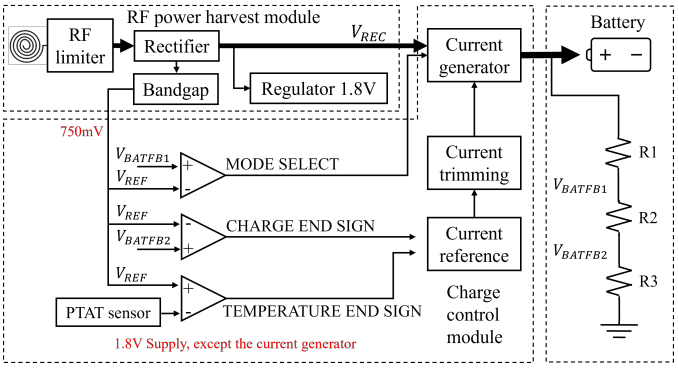

Fig. 7. System block diagram of the proposed on-chip wireless power charger.

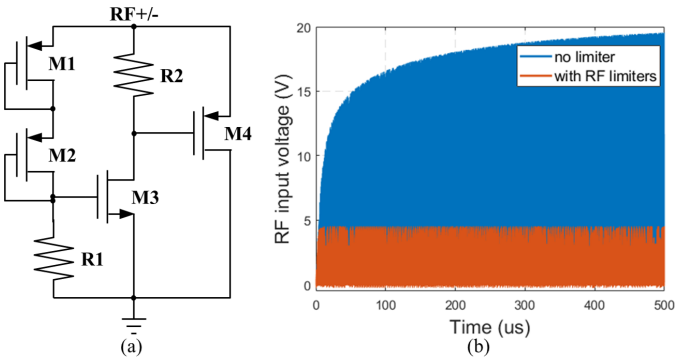

Fig. 8. (a) Schematic of an RF limiter. (b) Clipped inputs by the RF limiter.

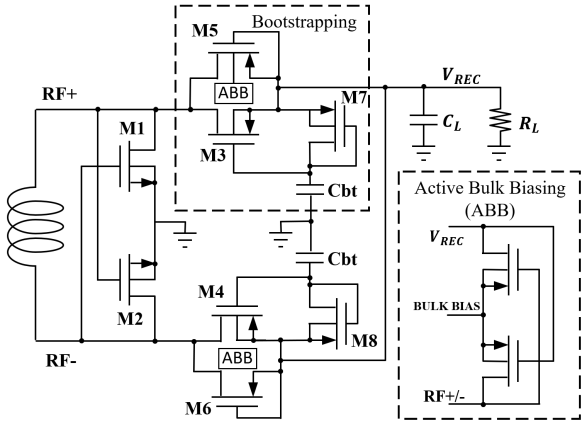

Fig. 9. Schematic of a full-wave rectifier with active bulk biasing and bootstrapping [31].

A. RF power harvesting module

1) RF limiter: All of these drawbacks justify the need to have an RF limiter to restrict the variations in the rectifier and also for impedance matching purposes. The used RF limiter [30] schematic is shown in Fig. 8(a). M1 and M2 are two diode-connected transistors that sense the voltage level of the RF inputs. Once the RF input exceeds the limited voltage, M3 will be turned on and pull down the gate voltage of the M4 to zero. After M4 is fully switched on, it forms a conduction path that allows the excess current to flow into the ground. M4 is designed with a large W/L ratio to ensure the current path and also stabilise the limited voltage level, independently of the increase in the RF inputs. Design simulations were set under extreme conditions, with the assumption of 20V RF input. As shown in Fig. 8(b), the RF input voltage level was efficiently kept below 4.5V.

2) Full-wave rectifier with active bulk biasing and bootstrapping technologies: In CMOS processes, conventional rectifiers are designed by diode-connected transistors (gate and drain are connected to allow devices to always operate in the saturation region) which convert the RF voltage signal to a DC voltage. However, the performance is limited by the threshold voltage of transistors and also their source-drain resistance. This results in a low power conversion efficiency (PCE) and voltage conversion efficiency (VCE). In this work, a semi-active full-wave rectifier with active-bulk control

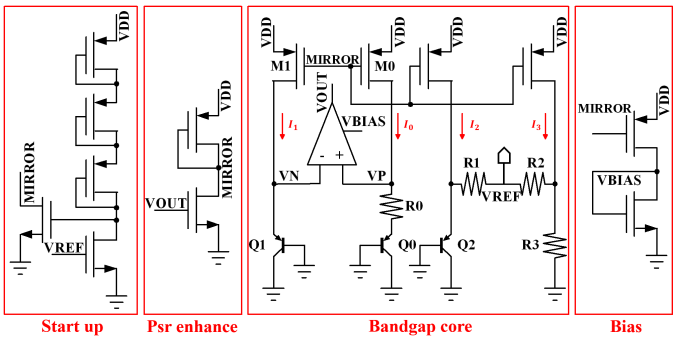

Fig. 10. Schematic of the proposed bandgap reference.

and bootstrapping was designed, as shown in Fig. 9. The bootstrapping structure on the M3/4 main branch was used to control for degradation in performance caused by leakage of the power transistors (M3/M4). Power transistors come with large width/length ratio and often have lower threshold voltage, leading to more complexity when trying to fully shutdown their current paths. Analysing further in detail the bootstrapping circuit composed of M3, M5, M7, C_{bt}, in the RF positive cycle, transistor M3 provides the main path to deliver the power to the load. Meanwhile, a small amount of power through diode-connected transistor M7 is used to charge the bootstrapping capacitor C_{bt}. M5, directly connecting input and output, biases the bootstrapping circuits. Keeping the size small limits the amount of current it can conduct to the output, hence its power loss contribution is negligible. Since the bootstrapping structure charges C_{bt} in the positive cycle, C_{bt} also biases the gate of M3 corresponding to its charging state, keeping the large potential difference between the gate node (the anode of C_{bt}) and the source node (the rectifier output). This provides reliable control to fully switch on and off the power path through M3, to reduce the leakage current from it, which leads to much higher efficiency in both voltage and power. The rectifier output V_REC is calculated in (20).

where V_{TH3} and V_{TH7} represent the threshold voltages of M3 and M7, respectively. Similarly, the bootstrapping circuit formed by M4, M6, M8, C_{bt}, biases the gate of the power transistor M4 to effectively switch off its power path to reduce the leakage current in the same manner. All transistors' bulks were connected to their source, except M5 and M6. The active bulk biasing technology kept M5/6's bulk at the highest potential level, preventing any latch-up damage caused by forward-biasing the bulks. As shown in the frame in Fig. 9, this was achieved using a simple cross-coupled inverter-based circuit. This compares the rectifier output with the RF inputs and outputs the higher input to the bulks to maintain them at a high voltage level. The used rectifier achieved 90% VCE and 89.3% PCE, with a 1kΩ resistor and a 100nF off-chip capacitor.

$$V_{REC} = V_{RF+} - (|V_{TH3}| - |V_{TH7}|) \tag{20}$$

3) Low power bandgap reference and low-dropout regulator: The proposed bandgap reference circuit is shown in Fig. 10. This design provides a low temperature coefficient (ppm), high power-supply rejection ratio (PSRR) reference voltage for regulators and a charge control module (as described in the next section). It consists of a start-up circuit, a PSRR enhancement circuit, the core bandgap function and biasing for the opamp.

The bandgap core circuit generates the temperature-independent reference voltage in a conventional way with the combination of the complementary to absolute temperature (CTAT) voltage V_{CTAT} and proportional to absolute temperature (PTAT) voltage V_{PTAT}. A two-stage opamp with a high gain was used to keep both VP and VN nodes at the same voltage level. By self-biasing the opamp with the current from BJT branches, its power consumption is greatly decreased, and also, the gain-bandwidth product is less sensitive to the supply variation. The output stage was a duplication of the core circuit. The I_0 and I_1 were replicated to the REF_L and REF_R branch generating another CTAT voltage V_{EB} through Q2, and PTAT voltage I_3R_3 through R_3. R_1 and R_2 have the same resistance, this being higher than other resistors to isolate the effects of I_2 and I_3 on the reference output. By trimming the resistance of R_1 and R_2, the circuit could output a customised reference voltage, rather than being fixed around 1.2V, to meet the zero temperature coefficient. The reference voltage VREF and its temperature coefficient are as calculated below,

$$V_{REF} = V_{EB} + I_R R_1 = I_3 R_3 + \frac{I_3 R_3 - V_{EB}}{R_1 + R_2} R_1 \tag{21}$$

$$\frac{\partial V_{REF}}{\partial V_T} = \frac{1}{2}\left(R_3 \frac{\partial I_3}{\partial T} + \frac{\partial V_{EB}}{\partial T}\right) \tag{22}$$

where I_3 is the current flowing in the REF_R branch, I_R is the current flowing through R_1 and R_2, and T is the temperature.

In order to achieve a high PSRR, a voltage subtractor was integrated into the output of the opamp. It formed a feedback loop, which modulates the gate voltage of the current mirror(M0, M1) with respect to their source node VDD (supply of the circuit from the rectifier output). Hence, the supply noise fed from the power source (VDD) to the opamp inputs (VN, VP) was effectively degraded by the output of the opamp. Due to the phase inversion generated from the voltage subtractor, the input connection of the opamp was reversed here.

The proposed bandgap reference could output 751mV of reference voltage with 9.3 ppm. Its quiescent current was 23.3μA, and its PSRR performance was enhanced to -78dB@1kHz and -50dB@1MHz. The LDO regulator was designed with a PMOS transistor as its pass element. A folded-cascode amplifier was used to regulate the 1.8V output. The quiescent current of the LDO was limited at 21.12μA to ensure its low power operation. It achieved a PSRR of -64.3dB@1MHz which was enough to prevent it from feeding power noise into charge control circuits.

B. Charging control module

The charging control module was designed following the NiMH battery charging flowchart depicted in Fig. 11, as per the NiMH handbook and its datasheet [32]. A four-stage

constant-voltage method was used to charge the battery continuously: (a) A soft-start stage with 450uA charging current when the battery level is below 2.4V (to prevent sudden current surges and ensure the battery is charging under a normal temperature range. It requires soft-start charging to warm up if the battery temperature is less than 0°C; (b) An accelerated stage with 3mA charging current when the battery is between 2.4V and 2.9V; (c) A trickle stage with 400uA charging current when the battery is nearly fully charged with its level over 2.9V; (d) A thermal shutdown stage that senses the state of the battery at all time and shuts down the charge current generator circuit when the battery temperature approaches 45°C.

The first three charge stages (a)(b)(c) were determined by comparing the battery voltage level with the bandgap reference voltage (750mV) in the power harvest module. All the comparisons were processed using 1MHz strong-arm latch comparators [33]. The battery level detection was done by implementing three serial feedback resistors R1, R2, R3, in parallel. The (a)(b)(c) charge stage comparisons are explained mathematically by in (23), (24) and (25). The feedback resistor can be calculated based on those equations, as shown in (26).

$$V_{BATFB1} = 2.4 \cdot \frac{R_2 + R_3}{R_1 + R_2 + R_3} < V_{REF}, \text{ soft-start} \quad (23)$$

$$V_{BATFB1} = 2.4 \cdot \frac{R_2 + R_3}{R_1 + R_2 + R_3} > V_{REF}, \text{ accelerate} \quad (24)$$

$$V_{BATFB2} = 2.9 \cdot \frac{R_3}{R_1 + R_2 + R_3} > V_{REF}, \text{ trickle} \quad (25)$$

$$R_1{:}R_2{:}R_3 = 319K{:}25K{:}120K \quad (26)$$

Meanwhile, a CTAT sensing circuit was also designed to detect the battery's temperature level. The PTAT circuit outputs a temperature-dependent voltage from 813mV to 686mV, associated with temperature rises from 0°C to 90°C. This is used to compare with the bandgap reference voltage in order to activate the temperature shutdown function.

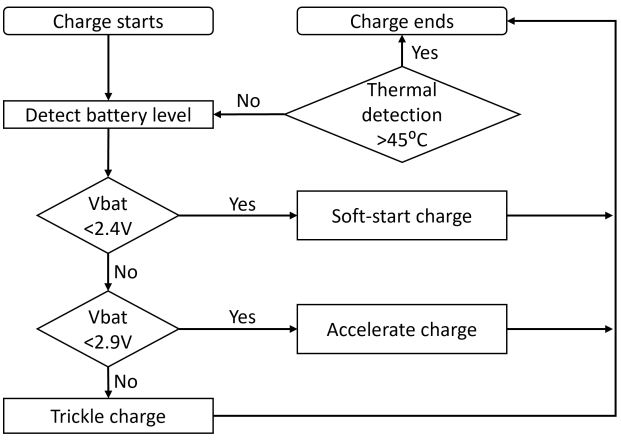

Fig. 11. The flowchart of the charge control module for a 2.4V 16mAh NiMH battery.

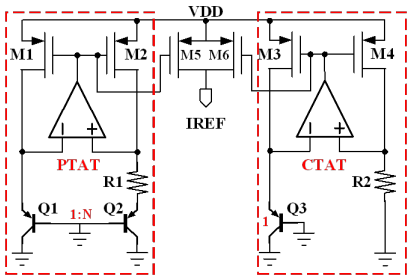

Fig. 12. Schematics of the current reference circuit.

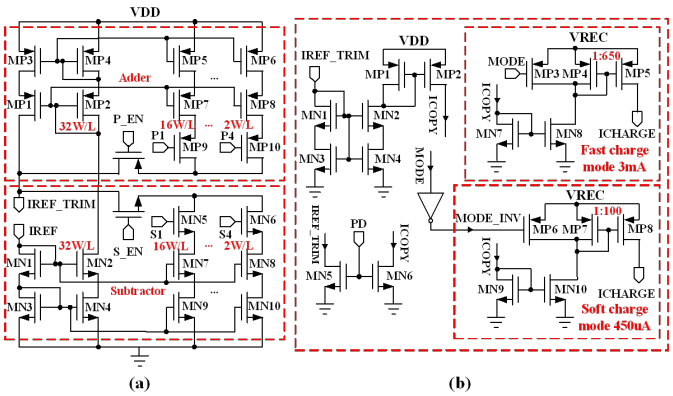

Fig. 13. Schematics of: (a) trimming circuit; (b) charge current generator with three mode switching functions.

1) Current reference: The proposed current reference circuit, as shown in Fig. 12, was used to ensure the stability and robustness of the charging process. It used an amplifier-based structure to generate the low temperature-coefficient current, IREF, by summing the PTAT current and the CTAT current. The circuit outputs 4.5μA with a temperature coefficient of 41.5ppm/°C in the typical (TT) corner.

2) Current trimming and generator circuit: To overcome the current reference error caused by process corner differences, a trimming circuit was designed here to adjust the charge current to the right level associated with the battery specifications. The circuit implementation is shown in Fig. 13(a). It uses two scaled cascade current mirror modules for the current adder function and the current subtractor function. The current addition and subtraction are controlled by pins P_EN, P1, P2, P3, P4, and pins M_EN, M1, M2, M3, M4, respectively. The ratios of the current mirror at the pin P1-P4 and M1-M4 branches to the IREF branch are 1:16, 1:8, 1:4 and 1:2, respectively. With the pin P_EN and M_EN activating the current trimming, the current reference could be adjusted from 2.1uA to 6.9uA, with steps of 0.15uA. The measurement results of the compensated current reference under each process corner were shown in Table IV, where X represents "does-not-matter". In the pin input, the pin sequence is P_EN, P4-P1, M_EN, M4-M1.

The proposed charge current generator is shown in Fig. 13(b). The current reference is replicated to the copied reference current ICOPY firstly to isolate the current reference with the next charge current generation. ICOPY is scaled up

TABLE IV
THE COMPENSATED CURRENT REFERENCE OUTPUT UNDER DIFFERENT PROCESS CORNERS.

Process corners	TT	FF	SS	SF	FS
IREF	4.5uA	5.01uA	4.07uA	4.49uA	4.51uA
ppm	41.5	49.6	29.5	39.8	43.1
Compensated IREF	4.5uA	4.52uA	4.48uA	4.49uA	4.51uA
Pin sequence	1XXXX 0XXXX	1XXXX 10011	01100 0XXXX	1XXXX 0XXXX	1XXXX 0XXXX

to the soft-start charge current at 450uA and accelerate charge current at 3mA by two current mirror circuits, with scaling ratios of 1:100 and 1:650, respectively. Transistors with a length of 2um are used to ensure replication accuracy. In order to achieve the charge mode switch function, pin MODE is added in parallel with the gate of their current mirrors to switch two charge current modes (soft-start mode and accelerated mode). Each replicated charge current branch was paired with one PMOS switch to achieve full switching ability. Trickle mode was achieved by placing a switch with a small W/L in parallel with the current reference output to partly close the current flow when the accelerated charging current is generated. Pin PD enables full shutdown of the charge current generator by pulling down the voltage to zero on both the input and output sides.

VI. RESULTS

A. Performance tradeoff simulation compliance with FCC regulations

Simulations were carried out to investigate system design tradeoffs that needed to be taken into account in order to comply with regulatory rules. Three model setups were simulated as follows:

a) Transmitter coil array placed under the mattress and no relay coils.
b) Transmitter coil array placed under the mattress and relay coil array inserted into the mattress at the height of 51mm.
c) Transmitter coil array placed under the mattress and relay coil array inserted into the mattress at the height of 76mm.

The tradeoffs are shown in Table V. The maximum permissible transmit power was measured once one the limits of regulations were hit. The near-field E-field strength of the three models was below the FCC limits because their measurement distance was less than the wavelength. Their near-field E-field could not be stabilised into the harmonic wave to strengthen its field. Compared with models (b) and (c), model (a) easily exceeded the FCC far-field limits even though its input power level (a) was ten times less than that of models (b) and (c). This was due to the presence of the relay coils. Their radiation pattern for far-field E-field strength was plotted in a cubic cavity with a side length of 60m. This is shown in Fig. 14. Due to the high Q-factor of relay coils, it was strongly coupled with the corresponding primary coils, reducing the free radiation in the EM field. Moreover, the relay coil had an identical non-coupling structure, further

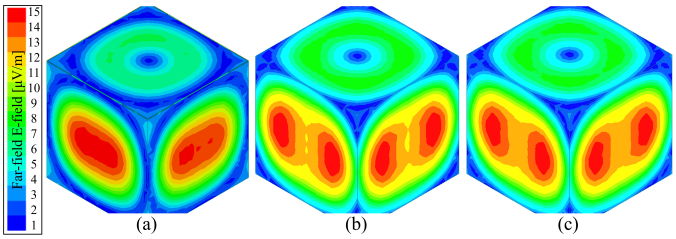

Fig. 14. Far-field E-field radiation pattern of three models under their maximum transmit power: (a) TX array placed under the mattress and no relay coils; (b) TX array placed under the mattress and relay coil array inserted into the mattress at the height of 51mm; (c) TX array placed under the mattress and relay coil array inserted into the mattress at the height of 76mm.

TABLE V
MAXIMUM PERMISSIBLE TRANSMIT POWER UNDER FCC RF AND SAFETY REGULATION LIMITS

Model	Maximum transmit power (W)	MPE @H-field (A/m)	MPE @E-field (V/m)	Far-field @E-field (μV/m)
(a)	0.08	0.05	0.225	15.1
(b)	1.4	0.355	0.325	15
(c)	1.2	0.590	1.651	15

enhancing the non-coupling field in the far-field and modifying the radiation pattern of the E-field.

To get better PTE performance, models (b) and (c) were simulated with the receiver coil aligned at different transmit distances. Their PTE results are shown in Fig. 15. Two vertical lines labelled the longest permissible distance under the FCC limits, delivering a fixed 10mW power to the receiver to ensure the wearable's operations. This was around 9.4cm for model (b) and 11.1cm for model (c). As expected, model (c) was shown to perform better PTE than the other two models. Moreover, an area of 60cm times 60cm takes into account patient's movement during the time spent in bed. This was considered to be a reasonable assumption taking into account the intended use is for patients who are not very active due to their inherent health conditions.

The power delivery distribution of the BCPT subsystem was simulated based on the configuration of the model (c). The results are shown in Fig. 16. The red area indicates the wearable can receive power of over 5mW to ensure its reliable operation, and the blue area indicates that the wearable can receive over 10mW. The outer part of the red area represents cancellation planes generated as a result of the chosen non-coupling coil pattern. As electromagnetic fields are nullified in the cancellation plane, the receiver placed there has minimal coupling with the primary-relay coils. Consequently, the BCPT subsystem cannot accurately detect its state and optimize power delivery. However, the cancellation plane only occupies a small part of the power transfer area and this could potentially be overcome in a future design by having more relay coils in the cancellation planes to enhance the PTE performance.

Unlike other state-of-the-art works that use fixed coil array configurations to generate uniform power distribution, the power(amplitude/phase) of each primary-relay coil in this work is controlled independently and adjusted in real time.

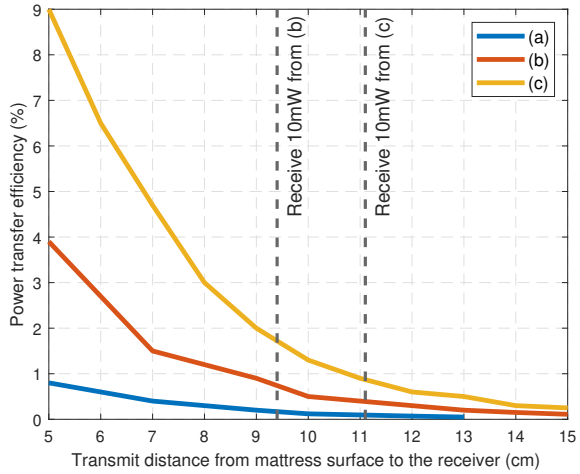

Fig. 15. PTE performance of models (a), (b) and (c); compliance with FCC regulations.

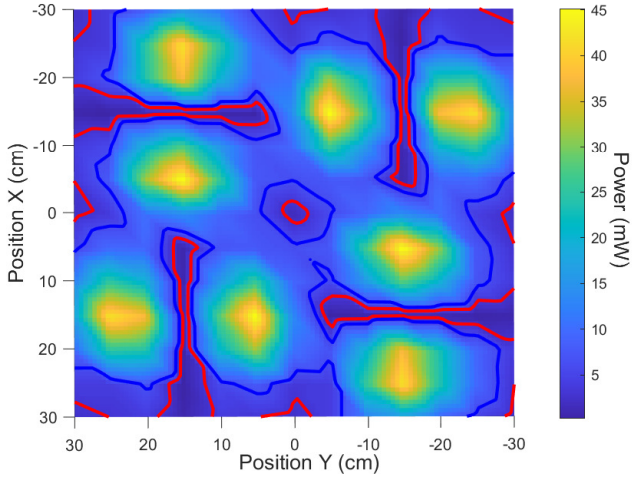

Fig. 16. Power delivery distribution over an area of 60cm times 60cm with wearable at a height of 8cm above the mattress.

The results obtained in simulation assumed that the transmitter is 12.7cm under the mattress and indicated that the receiver can harvest at least 5mW power in most places in the power delivery area of the system and up to 20.7cm of distance from the receiver. Moreover, if the receiver is closer to the mattress, it could harvest even more power, up to 100mW. Effectively this means that under the intended use conditions (within a RX-mattress distance of 8cm plus a TX-mattress distance of 12.7cm, and assuming a reasonable time in bed consistent with the needs of the type of patients), the BCPT subsystem can provide enough power to charge a small-capacity NiMH battery and maintain low-power sensors operating.

B. Experimental setup and results

The implemented BCPT subsystem is shown in Fig. 17. Its algorithm was run by an Arduino Due. Four AD8302 gain/phase detectors were used to detect the electric parameter of TxR at each primary coil input. An AD9959 RF signal generator and four THS3092DDA power amplifiers were used

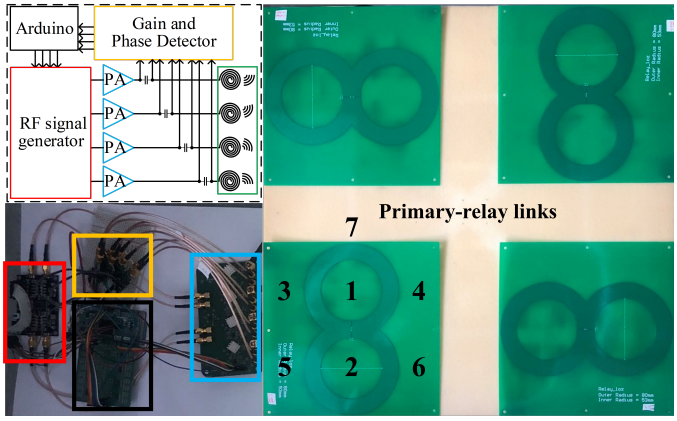

Fig. 17. PCB prototype of the BCPT subsystem (Relays are positioned on the top of the mattress for illustrative purposes).

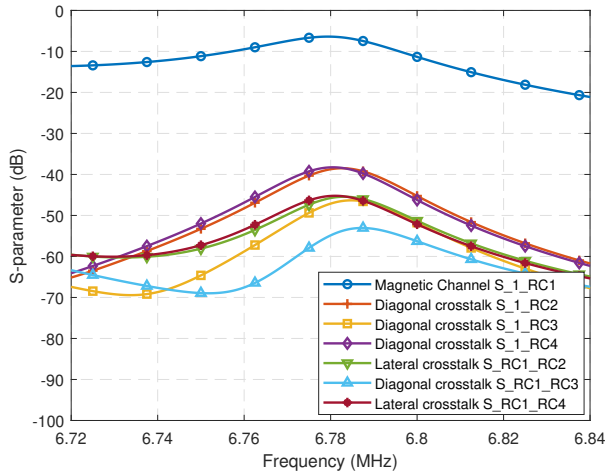

Fig. 18. Experimental measurements of the anti-crosstalk performance of the primary-relay link.

to feed the beamforming-controlled voltage with the right amplitude and phase to the corresponding primary coil inputs.

As shown in Fig. 18, the non-coupling coil array performance was measured by an HP8753D network analyser. S_1_RC1 represents the desired magnetic channel between Primary coil 1 and its corresponding relay coil RC1. It can be seen from their s-parameter (transmission coefficient) measurement that the non-coupling pattern attenuates the crosstalk from other lateral or diagonal coils by 30 decibels, made each TxR independent and helped the BCPT processing.

The proposed BCPT subsystem performance was measured under different positions of the receiver. The secondary coil in the receiver was matched with a 50Ω load and it was probed by an Agilent MSOX3054A 500MHz oscilloscope. Following the position labelled in Fig. 17, its PTE performance was measured at a maximum TX-RX distance of 20.7cm, indicating the worst scenario case that could happen. This is compared with the conventional MISO systems with equivalent inputs. After applying the BCPT algorithm, the PTE performance was significantly enhanced by 2-3 times, assuming wearables worn on the human body, as shown in Table VI. The PTE performance on position 7 appears

TABLE VI
PTE AGAINST POSITION MISALIGNMENT AT A MAXIMUM TX-RX DISTANCE OF 20.7CM, COMPARING EQUIVALENT INPUTS AND BEAMFORMING-CONTROLLED INPUTS.

Position	Equivalent input power/efficiency	Beamforming input power/efficiency
1 (aligned)	10.5mW (0.88%)	21.2mW (1.77%)
2 (aligned)	5.8mW (0.48%)	14.8mW (1.23%)
3 (misaligned)	2.5mW (0.21%)	6.1mW (0.5%)
4 (misaligned)	3.2mW (0.27%)	7.7mW (0.64%)
5 (misaligned)	2.2mW (0.18%)	5.4mW (0.45%)
6 (misaligned)	2.9mW (0.24%)	6.5mW (0.54%)
7 (misaligned)	1.2mW (0.1%)	3mW (0.25%)

degraded because of the existence of the cancellation plane induced by the nearby non-coupling coil.

Beamforming also improves efficiency across different coil rotation angles. In this prototype, it enhanced power delivery to the receiver up to a 45-degree rotation angle. However, for increased rotation, the efficiency would decrease, since as per Faraday's law of induction, the induced current will go down if the magnetic flux across the coil does.

The performance of this BCPT subsystem was compared with other state-of-the-art BCPT systems. This comparison is shown in Table VII. The PTE in the table corresponds to the AC-AC efficiency achieved between the primary and secondary coils. To facilitate a precise comparison in this specific application context, a figure of merit (FOM) is defined as follows:

$$FOM = \frac{PTE \cdot D}{A_{TX} \cdot A_{RX}} \tag{27}$$

where A_{TX} represents the total area of the primary coils, A_{RX} represents the total area of the secondary coils, and D represents the distance between the primary coils and the secondary coil. In addition to optimizing PTE performance and the power transfer distance between the coils, this figure of merit also considers the size of the coils because of the specific intended use covered by this work, in which the physical burden for the patient must be minimized. Although this work's FOM is relatively lower than certain state-of-the-art systems, it is important to notice that the PTE performance was intentionally reduced to comply with FCC/ICNIRP safety standards (detailed in Table III).

The proposed WPC was fabricated in TSMC 180nm technology. The chip micrograph is shown in Fig. 19. Its core area was 0.75mm^2. Fig. 20 shows the charging status during the soft-start, accelerated and trickle charge stages. It took around 8 hrs to fully charge a 16mAh NiMH battery without the charge adjustment. The power conversion efficiency was around 89.3%, and the power charge efficiency achieved 83.9% during charging.

VII. CONCLUSION

In conclusion, this paper presented a proof-of-concept wireless battery charging system targeting the typical energy needs of wearables intended to be used 24/7, without interruptions for charging, for application in physiological monitoring of patients that are guaranteed to spend a minimum of 8 hours in bed in between the time it would take from a full battery charge to battery depletion. The proposed BCPT subsystem was designed to adhere to globally accepted electromagnetic regulations, and effectively enhanced the power performance of traditional MISO systems. The simplified beamforming algorithm was able to render the power link more robust against coil misalignment whilst the achieved performance of the miniaturized receiver (4cm diameter) fulfils the power requirements of most wearables, particularly for continuous physiological monitoring applications.

Moreover, the proposed high-efficient WPC offered a reliable and safe method to charge a NiMH battery over time with 77.07% AC-DC efficiency. It's charging configuration could also be adjusted to be compatible with most NiMH batteries with small capacities. Overall, this proved the feasibility of a mattress-based wireless charging system to deliver enough energy to a wearable for physiological monitoring eliminating the need for separate charging.

Future research will investigate how to reduce the sensitivity of the PTE against coils misalignment in the non-coupling region, as well as how to further enhance the PTE, considering further integration of additional relay coil patterns in other regions to enhance the PTE locally.

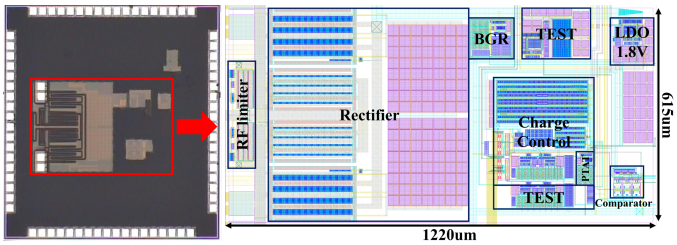

Fig. 19. Chip Micrograph of the proposed WPC.

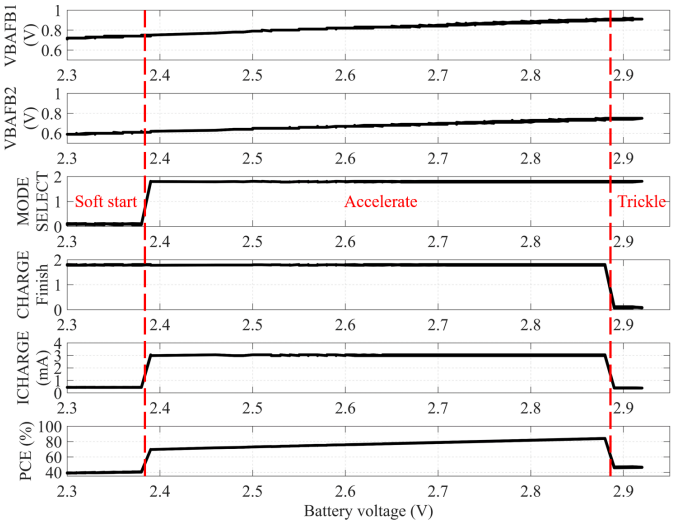

Fig. 20. Charge status measurement of the WPC chip.

REFERENCES

[1] M. C. Odden, P. G. Coxson, A. Moran, J. M. Lightwood, L. Goldman, and K. Bibbins-Domingo, "The impact of the aging population on coronary heart disease in the United States," (in eng), Am J Med, vol. 124, no. 9, pp. 827-33.e5, Sep 2011.

TABLE VII
COMPARISON OF STATE-OF-THE-ART WORKS ON MID-RANGE POWER CHARGING APPLICATIONS USING BCPT.

Ref.	Frequency (f)	Distance (D)	Primary/relay coil (ϕ is diameter)	Secondary coil	PTE	PDL	FOM	Does it pass FCC &ICNIRP regulation
[19]	6.78MHz	20cm	4 TXs with ϕ 20cm	A RX with ϕ 10cm	10%	-	20.26	Unknown
[20]	1MHz	45cm	6 TXs with total 0.38m^2	Multiple RXs with each area of 0.005m^2	15%	-	35.53	Unknown
[34]	1MHz	50cm	6 TXs with total 0.38m^2	A RX with area of 0.005m^2	11%	1W	28.95	Unknown
[35]	13.6MHz	8cm	4 TXs with ϕ 10.7cm	A RX with ϕ 10.7cm	45%	-	111.31	Unknown
[36]	1MHz	20cm	5 TXs with ϕ 20cm	four RXs with ϕ 4cm	34%	-	86.12	Unknown
[37]	6.78MHz	5cm	2 TXs	A RX	$\sim$80%	-	-	Unknown
[38]	-	30cm	16 TXs with ϕ 10cm 64 TXs with ϕ 10cm 256 TXs with ϕ 10cm	A RX with ϕ 4cm	30% 25% 10%	-	569.93 118.74 11.87	Unknown
[39]	6.78MHz	100cm	5 TXs with ϕ 20cm 3 relay coils with ϕ 20cm TX-Relay distance with 50cm	A RX with ϕ 20cm	73.59%	31.3W	149.12	Unknown
This work	6.78MHz	20.7cm	4 TXs with ϕ 15cm 4 relay coils with ϕ 15 cm	A RX with ϕ 4cm	1.77%	$>$20mW	39.85	Yes

[2] T. V. Boyko, M. T. Longaker, and G. P. Yang, "Review of the Current Management of Pressure Ulcers," (in eng), Adv Wound Care (New Rochelle), vol. 7, no. 2, pp. 57-67, Feb 1 2018.

[3] A. M. Jawad, R. Nordin, S. K. Gharghan, H. M. Jawad, and M. Ismail, "Opportunities and Challenges for Near-Field Wireless Power Transfer: A Review," Energies, vol. 10, no. 7, p. 1022, Jul. 2017, doi: 10.3390/en10071022.

[4] S. R. Khan, S. K. Pavuluri, G. Cummins, and M. P. Y. Desmulliez, "Wireless Power Transfer Techniques for Implantable Medical Devices: A Review," Sensors, vol. 20, no. 12, p. 3487, Jun. 2020, doi: 10.3390/s20123487.

[5] A. Tobola et al., "Sampling rate impact on energy consumption of biomedical signal processing systems," in 2015 IEEE 12th International Conference on Wearable and Implantable Body Sensor Networks (BSN), 9-12 June 2015 2015, pp. 1-6.

[6] Ziemssen, Tjalf et al. "Influence of ECG sampling frequency on spectral analysis of RR intervals and baroreflex sensitivity using the EUROBAVAR data set." Journal of clinical monitoring and computing vol. 22,2 (2008): 159-68. doi:10.1007/s10877-008-9117-0

[7] "IEEE Standard for Safety Levels with Respect to Human Exposure to Radio Frequency Electromagnetic Fields, 3 kHz to 300 GHz," IEEE Std C95.1, 1999 Edition, pp. 1-83, 1999.

[8] "IEEE Standard for Safety Levels with Respect to Human Exposure to Radio Frequency Electromagnetic Fields, 3 kHz to 300 GHz," IEEE Std C95.1, 1999 Edition, pp. 1-83, 1999.

[9] "Guidelines for Limiting Exposure to Electromagnetic Fields (100 kHz to 300 GHz)," (in eng), Health Phys, vol. 118, no. 5, pp. 483-524, May 2020.

[10] S. Park, "Investigating human exposure to a practical wireless power transfer system using and the effect about key parameters of dosimetry," (in eng), PLoS One, vol. 15, no. 8, pp. e0236929-e0236929, 2020.

[11] K. Finkenzeller and D. r. Muller, RFID handbook : fundamentals and applications in contactless smart cards, radio frequency identification and near-field communication, 3rd ed. ed. Chichester: Wiley, 2010.

[12] X. Wei, Z. Wang, and H. Dai, "A Critical Review of Wireless Power Transfer via Strongly Coupled Magnetic Resonances," Energies, vol. 7, no. 7, 2014.

[13] A. M. Jawad, R. Nordin, S. K. Gharghan, H. M. Jawad, and M. Ismail, "Opportunities and Challenges for Near-Field Wireless Power Transfer: A Review," Energies, vol. 10, no. 7, 2017.

[14] X. -Q. Zhu, Y. -X. Guo and W. Wu, "Investigation and Modeling of Capacitive Human Body Communication," in IEEE Transactions on Biomedical Circuits and Systems, vol. 11, no. 2, pp. 474-482, April 2017.

[15] Y. Alazzawi, K. Aono, E. L. Scheller and S. Chakrabartty, "Exploiting Self-Capacitances for Wireless Power Transfer," 2020 IEEE International Symposium on Circuits and Systems (ISCAS), Seville, Spain, 2020, pp. 1-1.

[16] S. A. Mirbozorgi, H. Bahrami, M. Sawan and B. Gosselin, "A Smart Multicoil Inductively Coupled Array for Wireless Power Transmission," in IEEE Transactions on Industrial Electronics, vol. 61, no. 11, pp. 6061-6070, Nov. 2014.

[17] Mirbozorgi, S.A., Maghsoudloo, E., Bahrami, H., Sawan, M. and Gosselin, B. (2020), Multi-resonator arrays for smart wireless power distribution: comparison with experimental assessment. IET Power Electronics, 13: 4183-4193.

[18] R. Saha, B. Roy Joy and S. A. Mirbozorgi, "Wireless Power Transmission with Uniform Power Delivery in the 3D Space of the Human Body using Resonators in Parallel," 2021 43rd Annual International Conference of the IEEE Engineering in Medicine & Biology Society (EMBC), Mexico, 2021, pp. 7268-7271.

[19] Y. Zhao, X. Li, Y. Ji, and C. Xu, "Random Energy Beamforming for Magnetic MIMO Wireless Power Transfer System," IEEE Internet of Things Journal, vol. 7, no. 3, pp. 1773-1787, 2020.

[20] L. Shi, Z. Kabelac, D. Katabi, and D. Perreault, "Wireless Power Hotspot that Charges All of Your Devices," presented at the Proceedings of the 21st Annual International Conference on Mobile Computing and Networking, Paris, France, 2015.

[21] IEC 60601-2-52:2009, "Medical electrical equipment — Part 2-52: Particular requirements for the basic safety and essential performance of medical beds."

[22] "Wireless Power Transfer. AirFuel Resonant Baseline System Specification (BSS)," Wireless Power Transfer. AirFuel Resonant Baseline System Specification (BSS), pp. 1-100, 2017.

[23] Mutashar, Saad & Hannan, M. A. & Samad, Salina & Hussain, Aini. (2013). Design of spiral circular coils in wet and dry tissue for bio-implanted micro-system applications. Progress In Electromagnetics Research M. 32. 181-200.

[24] Liang, Y., et al. (2019). "A review of rechargeable batteries for portable electronic devices." InfoMat 1(1): 6-32.

[25] H. -J. Kim, K. Kim, S. Han, D. -W. Seo and J. -W. Choi, "Nearly Non-Coupling Coil Array Allowing Many Independent Channels for Magnetic Communication," in IEEE Access, vol. 6, pp. 34190-34197, 2018.

[26] K. Kim, H.-J. Kim, and J.-W. Choi, "Magnetic beamforming with non-coupling coil pattern for high efficiency and long distance wireless power transfer," in 2017 Wireless Power Transfer Conference, WPTC 2017, May 10, 2017 - May 12, 2017, Taipei, Taiwan, 2017: Institute of Electrical and Electronics Engineers Inc., in WPTC 2017 - Wireless Power Transfer Conference.

[27] Federal Communication Commission, FCC Rules & Regulation for Title 47, pt. 2, $2.1093, Dec. 2013.

[28] P. Hasgall, E. Neufeld, M.-C. Gosselin, A. Klingenböck and N. Kuster, "Itis database for thermal and electromagnetic parameters of biological tissues version 2.2", September 26th, 2011.

[29] Bulletin, O., et al. (1999). Questions and Answers about Biological Effects and Potential Hazards of Radiofrequency Electromagnetic Fields.

[30] S. Hassouni and H. Qjidaa, "A design of analog VDD generator for passive UHF RFID Tag in 90 nm CMOS," International Journal of Microwave and Wireless Technologies, vol. 7, no. 5, pp. 507-513, 2015.

[31] S. S. Hashemi, M. Sawan, and Y. Savaria, "A High-Efficiency Low-Voltage CMOS Rectifier for Harvesting Energy in Implantable Devices," IEEE Transactions on Biomedical Circuits and Systems, vol. 6, no. 4, pp. 326-335, 2012.

[32] Energizer Brands, LLC. “Nickel Metal Hydride (NiMH) Handbook and Application Manual.”
[33] B. Razavi, ”The StrongARM Latch [A Circuit for All Seasons],” in IEEE Solid-State Circuits Magazine, vol. 7, no. 2, pp. 12-17, Spring 2015.
[34] J. Jadidian and D. Katabi, ”Magnetic MIMO: how to charge your phone in your pocket,” presented at the Proceedings of the 20th annual international conference on Mobile computing and networking, Maui, Hawaii, USA, 2014.
[35] K. Hamano, K. Ohtsuka, R. Tanaka, and K. Nishikawa, ”4×1 Multi-input single-output magnetic resonance beamforming wireless power transfer system,” in 2017 International Applied Computational Electromagnetics Society Symposium (ACES), 1-4 Aug. 2017 2017, pp. 1-2.
[36] G. Cao, H. Zhou, H. Zhang, J. Xu, P. Yang, and X. Li, ”Requirement-Driven Magnetic Beamforming for MIMO Wireless Power Transfer Optimization,” in 2018 15th Annual IEEE International Conference on Sensing, Communication, and Networking (SECON), 11-13 June 2018 2018, pp. 1-9.
[37] N. Kang, M. Liu, and C. Ma, ”A Phase-controlled Stacked-transmitter Wireless Power Transfer System for Magnetic Field Beamforming,” in 2019 IEEE PELS Workshop on Emerging Technologies: Wireless Power Transfer (WoW), 18-21 June 2019 2019, pp. 238-243.
[38] Z. Li and Z. Sun, ”Enabling Magnetic Beamforming in MIMO Wireless Power Transfer Using Reconfigurable Metasurface,” in GLOBECOM 2020 - 2020 IEEE Global Communications Conference, 7-11 Dec. 2020 2020, pp. 1-6.
[39] B. Ma, Y. Zhao, X. Li, Y. Ji, and C.-Z. Xu, ”Magnetic Beamforming Algorithm for Hybrid Relay and MIMO Wireless Power Transfer,” Cham, 2019: Springer International Publishing, in Wireless Algorithms, Systems, and Applications, pp. 225-234.

Zhiqiang Xu received B.Eng degree in electronic and communication engineering from the University of Sheffield, Sheffield, U.K., in 2018 and the M.Sc. degree in analogue and digital integrated circuit design from Imperial College London, London, U.K., in 2019. He is currently pursuing the Ph.D. degree at the Wearable Technologies Lab at Imperial College London. His research interests include array signal processing, analogue and radio-frequency integrated circuit design, and wireless system-on-chip (SoC) for biomedical sensors.

Esther Rodriguez-Villegas is a Professor (Chair) of Low-Power Electronics at Imperial College London, originally known for her engineering techniques to drastically reduce power in integrated circuits. She subsequently focused her research on life-science applications, founding the Wearable Technologies Lab. This lab specialises on both: creating innovative wearable medical technologies to improve management and diagnosis of chronic diseases; and neural interfaces to facilitate brain research whilst improving animals’ welfare. Esther is also a founder, co-CEO/CSO, of two active life-sciences companies, Acurable and TainiTec. And she has served in many prestigious international technical committees, including, but not limited, to the Administrative Committee of the IEEE Solid State Circuit Society, IEEE ISSCC, IEEE ISCAS, IEEE ESSCIRC. Esther has received many international recognitions and awards. Examples include an IET Innovation Award (2009), a global XPRIZE-award (2014), AAALAC 3Rs award, 2018, and a Silver Medal of the UK Royal Academy of Engineering (2020). She was also named the top scientist/engineer in Spain under the age of 36 in 2009 (Complutense award); and in 2020 she was elected a Fellow of the UK Royal Academy of Engineering.